CCFE
CULHAM CENTRE FOR FUSION ENERGY

UK Atomic Energy Authority

UKAEA-CCFE-PR(23)143

A. Matejunas, L. Fletcher, L. Lamberson

Image-Based Inertial Impact Test for Viscoelastic Constitutive Identification: A Digital Replica for Error Quantification

Image-Based Inertial Impact Test for Viscoelastic Constitutive Identification: A Digital Replica for Error Quantification

A. Matejunas, L. Fletcher, L. Lamberson

This is a preprint of a paper submitted for publication in Strain

Received: Added at production | Revised: Added at production | Accepted: Added at production

DOI: xxx/xxxx

FULL PAPER

Image-based Inertial Impact Test for Viscoelastic Constitutive Identification: A Digital Replica for Error Quantification

Andrew Matejunas[1] | Lloyd Fletcher[2] | Leslie Lamberson*[1]

[1]Department of Mechanical Engineering, Colorado School of Mines, Colorado, United States of America

[2]Fusion Technology Facility, United Kingdom Atomic Energy Authority, South Yorkshire, United Kingdom

Correspondence

*Leslie Lamberson. Department of Mechanical Engineering, Colorado School of Mines, Colorado, United States of America Email: les@mines.edu

Summary

Due to the strong rate dependence in their mechanical response, polymers find widespread use in applications subject to impact loading. However, characterizing these materials on microsecond time scales has proven challenging. Traditional experimental techniques rely on satisfying a number of limiting assumptions and typically do not provide direct measurements of the material parameters. Here, we propose a novel implementation of the Image-Based Inertial Impact (IBII) test to extract viscoelastic constitutive parameters on these microsecond time scales using the stress gauge implementation of the virtual fields method. We validate the experiment using a digital replica approach in which the constitutive parameters are first extracted on a finite element model of an IBII test on a viscoelastic material. The finite element data are then used to synthetically deform computer-generated grid images, which are then polluted with gray-level noise to simulate the images that would be captured in a real-life experiment. These images are processed identically to a physical experiment, and the identification is repeated using the full-field displacements extracted from the computer-generated images to determine the ideal processing parameters. Parameter identification was found to strongly depend on the processing parameters used to extract the kinematic fields from full-field images, emphasizing the need for computational validation before attempting a physical experiment to extract constitutive parameters. The IBII experimental method was found to be capable of simultaneously identifying the bulk modulus and the shear modulus along with their associated time constant.

KEYWORDS:

full-field measurements, grid method, high strain rate, time domain viscoelasticity, image-based inertial impact

1 | INTRODUCTION

The mechanical response of polymers typically exhibits a strong time dependence and consequently a strong dependence on strain rate[1]. Polymers are often subjected to high-rate loading, either in manufacturing, such as during machining, or in their final applications, such as protective helmets. For engineers to design and evaluate these processes and structures, robust material models must be developed and their associated constitutive parameters identified.

The time dependence of polymers is traditionally modeled using viscoelasticity[1–3]. To facilitate implementation in numerical modeling programs, these viscoelastic models commonly represent materials as a system of linear springs and viscous dashes, the most common examples being the generalized Maxwell or Wiechert model and the Kelvin chain[1,2,4–6]. In these models, the long-term response is considered to be linear elastic, and the time dependence characterized by a series of stiffnesses, each associated with a time constant that describes viscous behavior.

A classic technique used to identify the parameters of these viscoelastic models is the creep test, in which a step load is applied and the evolution of the strain in the specimen is measured over time. In practice, however, a load cannot be applied instantly and instead has an associated rise time, t_{rise}. Without detailed knowledge of the stress history, this rise time effectively limits the minimum identifiable time constant to approximately $10t_{\text{rise}}$. Additionally, wave propagation within the specimen also prohibits identification of time constants within the order of a wave transit time. Therefore, creep testing is predominantly limited to time scales greater than 10^0 seconds[3].

At shorter time scales, viscoelastic materials are normally characterized in the frequency domain using vibration and wave propagation based experimental techniques, with two common examples being dynamic mechanical analysis (DMA) and ultrasonic characterization, respectively. In a typical DMA test, a viscoelastic specimen is subjected to a sweep of periodic stress oscillations in a single deformation mode at various subresonant frequencies and temperatures. These experiments identify viscoelastic properties such as storage and loss modulus as functions of excitation frequency and/or temperature, and the time-dependent response can be calculated from the frequency domain[7]. In shear testing, DMA experiments are typically limited by instrumental resonances to direct observation of frequency to a maximum of 10^1 to 10^3 Hz, corresponding to a time scale of 10^{-3} s. However, these frequency ranges are often expanded using assumptions such as time-temperature superposition[3,8,9] or by carefully designing the test apparatus to target a specific class of materials[10]. For frequencies above the resonant frequency of the specimen, utrasonic methods are often utilized. In these techniques, the moduli of the material are inferred from the measured wave speed and known density of the sample material, and the loss tangent is calculated from the attenuation of the wave amplitude. These ultrasonic techniques provide the ability to measure viscoelastic response at frequencies exceeding 10^6 Hz, but a careful experimental design must be utilized to account for energy losses and the acoustic response of the transducer[3].

Furthermore, these ultrasonic experiments only probe very small strain amplitudes unless high-power ultrasonic loading is used at resonant frequencies paired with additional metrology, such as full-field quantitative imaging[11–13].

For more general high-rate materials characterization, impact experiments such as Kolsky (split-Hopkinson pressure) bars are often utilized. Typically Kolsky experiments are limited by the need to attain uniform one-dimensional deformation in a single deformation mode, as well as the need to suppress inertial effects to achieve stress equilibrium. In particular, the need to verify force equilibrium makes the characterization of materials at small strains, prior to yield, unreliable[14,15]. Additionally, classical Kolsky analysis based on stress equilibrium has been found to consistently overestimate the complex modulus of polypropylene, while a special non-equilibrium implementation was found to identify the complex modulus more accurately[16]. However, these experiments still provide information in a single deformation mode and are sensitive to bar material and specimen preparation.

With recent improvements in ultra-high-speed (UHS) cameras and quantitative full-field imaging techniques, new methods have been developed and implemented that utilize full-field deformation measurements to relax many of the assumptions present in classical mechanical testing[17]. One such method is the image based inertial impact (IBII) test, discussed in detail in Section2, which leverages the inertial effects and heterogeneous deformation fields, which are typically suppressed in other dynamic experiments to identify constitutive parameters[18]. The IBII test method has been used in the literature to extract constitutive parameters for a variety of materials with numerous constitutive models. The technique was first validated with isotropic linear elastic materials[19,20], and used to identify the high-rate elastic properties of a tungsten carbide cermet[20]. Additionally, IBII experiments have been used to characterize the high-rate behavior of orthotropic fiber reinforced composites[21,22]. Strain rate dependence has also been investigated for metal plasticity[23,24]. However, to date, rate dependence has been insufficiently characterized in the elastic regime and strain rates are typically reported as either an average strain rate over the duration of the experiment or as the maximum strain rate achieved, despite the inherent heterogeneity of the measured strain rate fields. Here, we utilize the evolving strain rate fields inherent in the IBII method to extract the time-dependent properties of a viscoelastic material.

In this study, we present the framework for a novel implementation of the IBII test method for the identification of high-rate viscoelastic constitutive parameters in the time domain. Additionally, we validate the experimental method using a digital replica approach in which the specimen deformation is simulated using a finite element simulation, and data collection is simulated through the deformation of computer-generated grid images. Constitutive parameter identification is then validated through processing the resulting images in the same manner as a physical experiment.

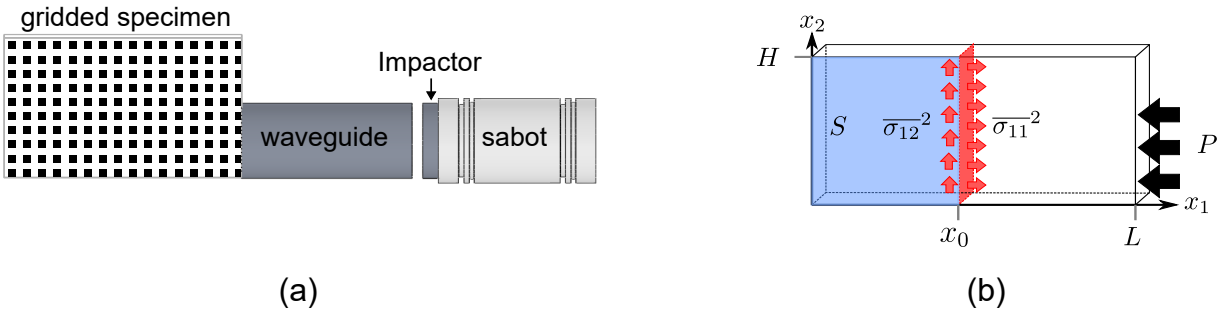

FIGURE 1 Schematic representations of (a) an IBII experimental setup and (b) the calculation of average in-plane stresses in an IBII experiment using the stress gauge equations.

2 | THE IMAGE BASED INERTIAL IMPACT TEST

In an IBII experiment, presented schematically in Figure 1(a), the impact of a projectile on a waveguide is used to impart a plane-stress wave in a thin plate specimen bonded edge-on to the waveguide. The propagation and interactions of the stress wave with the specimen boundaries generate a heterogeneous deformation field in the material. To measure these deformations, the specimen is instrumented with an UHS camera and a quantitative full-field imaging method, most commonly the grid method[25]. The measured displacement field is then differentiated in space and time to obtain full-field in-plane strains and accelerations, and the resulting kinematic fields are input into the virtual fields method (VFM), described in Sections 2.1 and 2.2, to extract material properties. In contrast to Kolsky bars, which are designed to minimize inertial effects, the use of the VFM in the IBII test leverages the inertial effects and allows for the use of the measured accelerations as a dynamic load cell. Additionally, while Kolsky bars require uniform deformation, the accuracy of the VFM improves with increasingly heterogeneous kinematic fields. Kolsky bars also typically provide only a point measurement in a single deformation mode, but if the impact occurs over only a portion of the specimen height, the IBII experiment can provide full-field deformation information in compression, tension, and in-plane shear[26,27].

2.1 | The virtual fields method

To obtain constitutive parameters from full-field displacement data, an inverse identification procedure must be applied to the kinematic fields obtained from an IBII experiment. The VFM is one such method that is based on the principle of virtual work. The principle of virtual work, derived from the weak form of the equation of motion, is given by:

$$-\int_V \sigma_{ij}\varepsilon^*_{ij}dV + \int_S T_i u^*_i dS + \int_V b_i u^*_i dV = \int_V \rho a_i u^*_i dV. \tag{1}$$

Here, the volume integral of the stress, σ_{ij} contracted with a virtual strain field, ε^*_{ij}, is the internal virtual work. The external virtual work is given by the surface integral of the external tractions, T_i, contracted with the virtual displacement field, u^*_i, added

to the volume integral of the body forces, b_i, contracted with the virtual displacement field. In IBII experiments, the body forces are composed only of gravity and have negligible magnitude reducing the external virtual work to $\int_S T_i u_i^* dS$. The sum of the internal and external virtual work equals the inertial virtual work given by the specimen density, ρ, multiplied by the volume integral of the acceleration filed, a_i, contracted with the virtual displacement. In these expressions the virtual fields, u^* and ε^*, are related with the strain–displacement relations for the infinitesimal strain tensor, $\varepsilon_{ij} = \left(u_{i,j} + u_{j,i}\right)/2$. These virtual fields serve purely as mathematical test functions without any physical meaning. u^* can be any continuous and piece-wise differentiable test function which satisfies the experimental boundary conditions and kinematic admissibility[28]. For an incompressible specimen, with the exception of ρ, all variables in Equation (1) are field variables and functions of space and time. The functional notation has been omitted here for simplicity.

In an IBII experiment, the quantitative full-field imaging technique allows for time-resolved measurements of in-plane displacements. These displacements can then be differentiated twice in time to obtain a_i and spatially differentiated to obtain strain. σ_{ij} cannot be directly measured and can instead be expressed as some function, $\sigma_{ij} = \sigma(\varepsilon_{ij}, Q)_{ij}$, of strain and the constitutive parameters, Q. However, due to the limitations of imaging techniques, these measurements for ε_{ij} and a_i, can only be obtained on the surface. Therefore, the test must be designed such that the assumptions of 2D plane-stress and uniform kinematic fields throughout the material thickness are satisfied. In the IBII experiment, these requirements are addressed through impacting a thin plate specimen along the edge.

The aforementioned two dimensional assumptions, along with an additional assumption of homogeneous material properties throughout the specimen, allow for Equation (1) to be rewritten in terms of surface integrals,

$$-\int_S \sigma\left(\varepsilon_{ij}, Q\right)_{ij} \varepsilon_{ij}^* dS + \int_S T_i u_i^* dS = \rho \int_S a_i u_i^* dS, \tag{2}$$

across the 2D surface of the specimen. For a material characterized by a linear elastic constitutive model, Equation (2) yields a linear system of equations that can be directly solved to obtain the constitutive parameters, Q. However, for nonlinear constitutive models where stress cannot be described as an explicit function of strain, such as those describing viscoelasticity, a cost function must be created and minimized in order to extract the model parameters. The process of generating and solving the cost function for this case is outlined in Section 2.4.

2.2 | Choice of virtual fields: the stress gauge equations

Despite the availability of an infinite number of virtual fields that satisfy the experimental boundary conditions along with the continuity, differentiability, and kinematic admissibility requirements, the choice of particular virtual fields remains an important consideration in the design of IBII experiments. A number of potential options for virtual fields in IBII tests have been explored in the literature including: manually defined polynomial fields[19–22,27,29,30], special optimised virtual fields, algorithmically

generated to reduce the impact of noise[20,28,29,31]; sensitivity-based virtual fields, computer-generated according to the sensitivity of stress fields to each constitutive parameter[23,24,32]; and the so-called stress gauge virtual fields that allow the accelerations to be used as a load cell without assuming the form of the constitutive model[29]. In this work, the stress gauge virtual fields are selected as a good starting place for multi-parameter viscoelastic parameter identification. Future investigations will study the impact of the choice of the particular form of the virtual fields on identification accuracy.

The full derivation of the stress gauge equations has been described in detail in literature[22], so it is only briefly recounted here. The stress gauge approach utilizes virtual displacement fields that yield null virtual strains. This virtual field choice cancels out the internal virtual work term. Therefore, Equation (2) reduces to:

$$\int_S T_i u_i^* dS = \rho \int_S a_i u_i^* dS. \tag{3}$$

The virtual fields allowing for the calculation of axial and in-plane shear stresses consist of rigid-body translations along the $\mathbf{x}_1$ and $\mathbf{x}_2$ axes, respectively. The specimen is then discretized into a series of vertical slices, as displayed by the red cross section in Figure 1(b), some distance x_0 from the free surface opposite the impact. Taking the cross product of the traction vector, T_i with the surface normal vector of the cross section at x_0 gives the normal stress component in the $\mathbf{x}_1$ direction, σ_{11}, as well as the in-plane shear stress σ_{12} on the internal cross section x_0. The integral can then be approximated as discrete sums over the portion of the field of view from $\mathbf{x}_1 = 0$ to x_0. With these substitutions Equation (3) can be evaluated with each virtual field to yield expressions for the average stresses along the cross section

$$\overline{\sigma_{11}}(x_0) = \rho x_0 \overline{a_1}^S. \tag{4a}$$

$$\overline{\sigma_{12}}(x_0) = \rho x_0 \overline{a_2}^S. \tag{4b}$$

Here, $\overline{a_i}^S$ represents the average acceleration in the $\mathbf{x}_i$ direction measured over the surface, highlighted in Figure 1(b) in blue, between the free edge at $\mathbf{x}_1 = 0$ and the cross section at x_0.

Together, Equations (4a) and (4b) make up the stress gauge equations for axial and shear stress. These equations allow for the calculation of specimen stress averages from measured displacements before assuming a particular form of the constitutive equations. For linear elasticity, the constitutive parameters can be identified by fitting the average stress–strain curves. However for viscoelastic and other nonlinear material models, a cost function comparing the stresses obtained through the stress gauge equations with those predicted by the constitutive model must be generated and minimized. In addition to the previously mentioned studies utilizing the IBII experiment, this non-parametric method for stress measurement has been used in other configurations for the characterization of rubbers[33,34], spall strength in concrete[35], and polymeric foams[36]. The particular procedure used to extract the constitutive parameters using these stress gauge equations is further described in Section 2.4

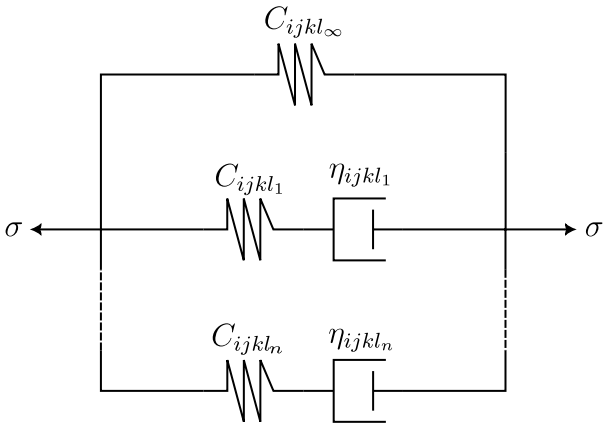

FIGURE 2 A schematic Representation of the generalized Maxwell model for viscoelasticity

2.3 | Constitutive Model: the Maxwell formulation of the standard solid model

In this investigation, the mechanical response of a viscoelastic material is modeled using the Maxwell formulation of the standard solid model, also known as the Zener Model[4,37]. In the model, a linear spring with a stiffness tensor, C_{ijkl_∞}, defines long-term mechanical response while a Maxwell element in parallel with C_{ijkl_∞} describes the time-dependent behavior. This Maxwell element consists of a linear spring with stiffness C_{ijkl_1} in series with a viscous dash-pot with damping constant η_{ijkl_1}. A time constant, τ_{ijkl_1} describes the relaxation of the elemental stiffness and relates the stiffness and damping through $\tau_{ijkl_1} = \frac{C_{ijkl_1}}{\eta_{ijkl_1}}$. The standard solid model can be further expanded into the generalized Maxwell model, schematically in Figure 2, to better describe more general viscoelasticity through the addition of further Maxwell elements in parallel to model the time dependence across a wider range of time scales[1,2]. Many commercial finite element software packages, such as Abaqus[6], implement their native viscoelasticity models with this generalized Maxwell model.

To build the cost function and extract constitutive parameters, the stress components σ_{11} and σ_{12}, must be reconstructed from measured in-plane strains using the constitutive model. The stress reconstruction is performed using the numerical algorithm developed by Mun[38],

$$\sigma_{ij}(t_{n+1}) = C_{ijkl_0}\varepsilon_{kl}(t_{n+1}) - \sum_{m=1}^{M} C_{ijkl_m}\left\{ \varepsilon_{kl}(t_n) + \exp\left(-\frac{\Delta t}{\tau_m}\right)\left[\varepsilon_{kl_m}(t_n) - \varepsilon_{kl}(t_n)\right] - \Delta\varepsilon_{kl}(t_{n+1})\left[1 - \frac{\tau_m}{\Delta t}\left[1 - \exp\left(-\frac{\Delta t}{\tau_m}\right)\right]\right]\right\} \tag{5a}$$

$$\varepsilon_{kl_m}(t_n) = \varepsilon_{kl}(t_{n-1}) + \exp\left(-\frac{\Delta t}{\tau_m}\right)\left[\varepsilon_{kl_m}(t_{n-1}) - \varepsilon_{kl}(t_{n-1})\right] + \frac{\Delta\varepsilon_{kl}(t_n)}{\Delta t}\left[\Delta t - \tau_m\left[1 - \exp\left(-\frac{\Delta t}{\tau_m}\right)\right]\right]. \tag{5b}$$

Here, the instantaneous stiffness, C_{ijkl_0} is defined as $C_{ijkl_0} = C_{ijkl_\infty} + \sum_{m=1}^{M} C_{ijkl_m}$.the in-plane strain components ε_{11}, ε_{22}, and ε_{12} are obtained directly from the measured displacement fields using the strain-displacement relations. The time step t_n

represents the current time starting at $n = 1$ and $t = 0$ with the next time step given by t_{n+1} and the previous by t_{n-1}, and $\Delta t = t_{n+1} - t_n = t_n - t_{n-1}$. The incremental creep strains are given by ε_{kl_m} with $\varepsilon_{kl_m} = 0$ at $t = 0$, and the time dependent response of each Maxwell element are summed over the total number of Maxwell elements, M, to determine the total time dependent response of the material.

Calculation of σ_{11} using Equations 5a and 5b requires out-of-plane strains, ε_{33}. However, an IBII experiment with a single camera cannot measure the out-of-plane displacements required to obtain the through thickness strains in the same manner as the in-plane strain. Instead, the plane stress assumption, $\sigma_{33} = \sigma_{13} = \sigma_{23} = 0$, was used to solve Equation5a for ε_{33} giving

$$\varepsilon_{33}(t_{n+1}) = \frac{\sigma_{\text{creep}}(t_{n+1})}{C_{3333_{\text{relax}}}(t_{n+1})}, . \tag{6}$$

Here, σ_{creep} is the effective out-of-plane creep stress, and $C_{3333_{\text{relax}}}$ is the relaxation of the C_{3333} component of the stiffness tensor over the time increment Δt. These terms are calculated with

$$\begin{aligned}\sigma_{\text{creep}}(t_{n+1}) =& \sum_{m=1}^{M}\Bigg[C_{3311_m}B_{11_m} + C_{3322_m}B_{22_m} + C_{3333_m}\left[\varepsilon_{33}(t_n) + \exp\left(\frac{-\Delta t}{\tau_m}\right)\left[\varepsilon_{33_m}(t_n) - \varepsilon_{33}(t_n)\right]\right] \\ & -\varepsilon_{33}(t_n)\left[1 - \frac{\tau_m}{\Delta t}\left(1 - \exp\left(-\frac{\Delta t}{\tau_m}\right)\right)\right] - C_{3311_0}\varepsilon_{11}(t_{n+1}) - C_{3322_0}\varepsilon_{22}(t_{n+1})\Bigg]\end{aligned} \tag{7a}$$

$$C_{3333_{\text{relax}}} = \left[C_{3333_0} - C_{3333_m}\sum_{m=1}^{M}\left[1 - \frac{\tau_m}{\Delta t}\left(1 - \exp\left(-\frac{\Delta t}{\tau_m}\right)\right)\right]\right]^{-1} \tag{7b}$$

$$B_{ij_m} = \varepsilon_{ij}(t_n) + \exp\left(-\frac{\Delta t}{\tau_m}\right)\left[\varepsilon_{ij_m}(t_n) - \varepsilon_{ij}(t_n)\right] + \left[\varepsilon_{ij}(t_{n+1}) - \varepsilon_{ij}(t_n)\right]\left[1 - \frac{\tau_m}{\Delta t}\left(1 - \exp\left(-\frac{\Delta t}{\tau_m}\right)\right)\right] \tag{7c}$$

In this feasibility study, we focus on the simplest case, using an isotropic material where the long-term response is known and the time dependence is governed by a single Maxwell element with unknown properties. For simplicity and consistency with the ABAQUS implementation of viscoelasticity, the remainder of this work describes stiffness tensors in terms of bulk and shear modulus, K and G. These moduli relate to C_{ijkl} through the standard relation between isotropic elastic constants, $C_{ijkl} = K\delta_{ij}\delta_{kl} + G\left(\delta_{ik}\delta_{kl} + \delta_{il}\delta_{jk} - \frac{2}{3}\delta_{ij}\delta_{kl}\right)$, where δ is the Kronecker delta. The IBII experimental technique proposed and analyzed in this investigation is designed to extract the elemental moduli K_1 and G_1 along with their associated time constant τ_1 from time-resolved full-field deformation data.

2.4 | Constitutive parameter identification

To identify the constitutive parameters from measured time-resolved full-field deformation information two cost functions, ϕ_{ij}, are implemented:

$$\phi_{12}\left(G_1, \tau_1\right) = \sum_X \sum_t \left(\overline{\sigma_{12}^{\text{Model}}} - \overline{\sigma_{12}^{\text{SG}}}\right)^2, \tag{8a}$$

$$\phi_{11}\left(K_1, G_1, \tau_1\right) = \sum_X \sum_t \left(\overline{\sigma_{11}^{\text{Model}}} - \overline{\sigma_{11}^{\text{SG}}}\right)^2. \tag{8b}$$

In these functions, the superscripts $^{\text{SG}}$ and $^{\text{Model}}$ indicate stresses obtained directly using the stress gauge equations in (4), and from the constitutive model in Equations (5-7) using measured strains and trial constitutive parameters.

The extraction of G_1 independent of K_1 is performed first by minimizing ϕ_{12} using the interior-point algorithm in MATLAB's[39] fmincon function. Here, G_1 and τ_1 are allowed to float, and the shear modulus and associated time constant are then obtained when the trail parameters create a global minimum in ϕ_{12}. This independent determination of G_1 without K_1 is possible because the shear response can be calculated without knowledge of bulk deformations or behavior.

However, the inverse does not hold and the shear modulus must be known in order to calculate the volumetric strain from measurements of only in-plane deformations. In ϕ_{11}, G_1 is fixed at the values identified from the minimization of ϕ_{12} while K_1 and τ_1 are allowed to float and are extracted through minimizing ϕ_{11} in the same manner as the minimization of ϕ_{12}. Due to the coupling of K_1 and G_1 in the calculation of $\sigma_{11}^{\text{Model}}$, final identification of τ_1 is performed through the minimization of ϕ_{11}. To confirm that cost functions converge on global minima, the procedure is repeated with three distinct sets of initial guesses within the expected order of magnitude as the constitutive parameters, and the parameters resulting in the minimum values for ϕ_{12} and ϕ_{11} are the identified constitutive parameter.

3 | NUMERICAL VERIFICATION

3.1 | Finite element model

A finite element model of the proposed IBII experiment configuration has been developed and implemented in Abaqus Explicit. Figure 3 presents a schematic representation of the model. The 2D model was constructed assuming plane-stress with an assumed thickness of 4 mm and the element properties listed in Table 1. Meshing was performed automatically with 4 node reduced integration (CPS4R[6]) elements and the simulation time step was allowed to float at $0.8t_{\text{crit}}$ where t_{crit} is the minimum transit time of a longitudinal wave in an element. Mesh convergence is confirmed when the calculated stress gauge stresses, and the average stresses output by Abaqus converged at all time steps and $\mathbf{x}_1$-coordinates.

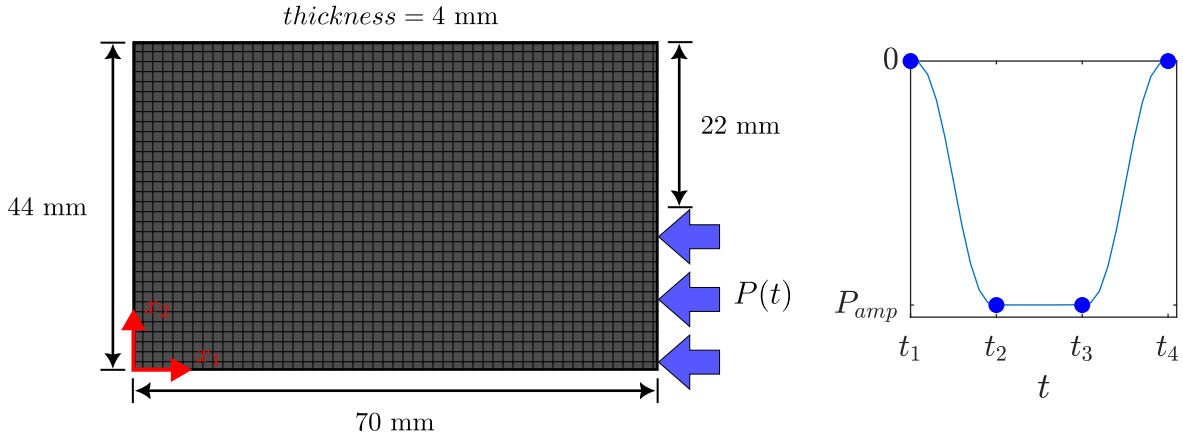

FIGURE 3 A schematic representation of a finite element model for a half height IBII experiment subjected to a compressive trapezoidal input pulse.

Finite Element Parameters			Long-Term Parameters		Maxwell Parameters		
Element Size (mm)	# Elements	Element Type	K_∞ (GPa)	G_∞ (GPa)	$K_{1_{\text{ref}}}$ (GPa)	$G_{1_{\text{ref}}}$ (GPa)	$\tau_{1_{\text{ref}}}$ (µs)
0.1	700×440	CPS4	2.07	1.18	1.53	0.877	10.0

TABLE 1 Finite element properties and reference constitutive parameters used for a finite element simulation of a material loosely based on experimental image based inertial release data for PMMA[40] and described by a single element generalized Maxwell model.

The material is defined by the Maxwell formulation of the standard solid model with the parameters listed in Table 1. The long-term moduli are based on quasistatic properties measured in image-based inertial release experiments performed on polymethyl methacrylate (PMMA)[40]. Similarly, the instantaneous response is based on the measured response at $\dot{\varepsilon} \approx 10^2$ s^{-1}. These input parameters are not intended to predictively model PMMA, but are intended to provide a reasonable baseline for constitutive parameter identification governing the time-dependent mechanical response.

The transmission of the incident stress wave into the specimen is modeled by applying a uniform trapezoidal pressure pulse, with a maximum amplitude of $P_{amp} = 60$ MPa, along half the specimen height. The pulse shape is defined by equal rise, dwell, and fall times, $t_{\text{rise}} = t_2 - t_1 = t_{\text{dwell}} = t_3 - t_2 = t_{\text{fall}} = t_4 - t_3 = 10$ µs. The pulse is applied with the smooth-step function in Abaqus approximating the ramps as a smoothly varying cubic function over t_{rise} and t_{fall}. Impacting over half of the specimen height allows for the generation of shear stresses on the same order of magnitude as the axial stresses in an isotropic material.

3.2 | Model Verification

To verify the implementation of the stress gauge formulation of the virtual fields method, as well as to check the convergence of the finite element model, the $\overline{\sigma_{11}}$ and $\overline{\sigma_{12}}$ calculated with the stress gauge equations were compared against those average

stresses calculated from the output of the finite element simulation. To better visualize the error patterns, a normalized error

$$\left\| \text{Error}\left(\overline{\sigma_{ij}^{\text{SG}}}\right) \right\|_{\max} = \frac{\overline{\sigma_{ij}^{\text{SG}}} - \overline{\sigma_{ij}^{\text{FE}}}}{\max\left(\overline{\sigma_{ij}^{\text{FE}}}\right)} \times 100. \tag{9}$$

was calculated. Here, $\max\left(\overline{\sigma_{ij}^{\text{FE}}}\right)$ is the maximum value of the width averaged stress, which is used to normalize the error and enable comparisons across the range of stress magnitudes. This normalization is indicated by $\|\|_{\max}$. The superscript $^{\text{FE}}$ denotes a kinematic field that is taken directly from the finite element output.

Figure 4(a) and (b) show the width averaged stress magnitudes output by the finite element simulation as functions of time, t, and distance from the free edge, x_0. To simulate the temporal resolution of a Shimadzu HPV-X1 UHS camera, 128 frames of strain and acceleration data were extracted every half microsecond for a simulated frame rate of 2 Mfps and a total experiment duration of 63.5 μs. The half-height trapezoidal pulse imparts a compressive loading with an amplitude of $\overline{\sigma_{11}^{\text{FE}}}^{\mathbf{x}_2} = 30$ MPa. As the wave propagates towards the free surface, the stress attenuates and loses its trapezoidal shape due to a combination of relaxation of the Maxwell moduli and the two-dimensional propagation of the stress wave. When the wave reflects from the free surface, it propagates back towards the impact edge reloading a portion of the specimen in tension. The shear stress follows a similar pattern, but with more pronounced spatial dispersion because shear stress is generated at single point on the edge of the applied pressure pulse.

Figure 4 (c) and (d) present the normalized errors in the calculation of width-averaged stresses using the stress gauge equations with finite element output acceleration fields. These error plots show an agreement in time and space between the stresses calculated with the stress gauge equations and those output by the finite element simulation within ±1.5% of $\max\left(\overline{\sigma_{11}^{\text{FE}}}\right)$ and ±1.0% of $\max\left(\overline{\sigma_{12}^{\text{FE}}}\right)$. However, localized bands of error exist in the calculation of $\overline{\sigma_{ij}^{\text{SG}}}^{\mathbf{x}_2}$, particularly in areas with significant temporal gradients in the stress magnitude. For example, errors in axial stress are most pronounced during the pulse rise and unloading closer to the impact edge with $\overline{\sigma_{11}^{\text{SG}}}^{\mathbf{x}_2}$ slightly lagging $\overline{\sigma_{11}^{\text{FE}}}^{\mathbf{x}_2}$. These errors likely stem from the reduced temporal resolution of the output compared to the finite element time step. However, as further investigation demonstrates, these errors do not significantly impact the identification. Additionally, the less than ±1.5% difference between the stresses from the finite element model and stress gauge equations indicates convergence of the finite element mesh.

The stresses output by these stress reconstruction algorithms from equations (5) to 7 are compared to those directly output from the finite element model in the same manner as in 9, and Figure 4 (e) and (f) present the resulting normalized errors. The errors in stress reconstruction follow a similar pattern to the stress gauge stresses with error concentrated when significant temporal gradients in stress exist. This agreement suggests that the source is also due to temporal integration issues, resulting in poor reconstruction at the transitions in the slope of the pulse in this case. This stress reconstruction error is on the same order as the discretisation error of the simulation, verifying the reconstruction algorithm for use in constitutive parameter identification.

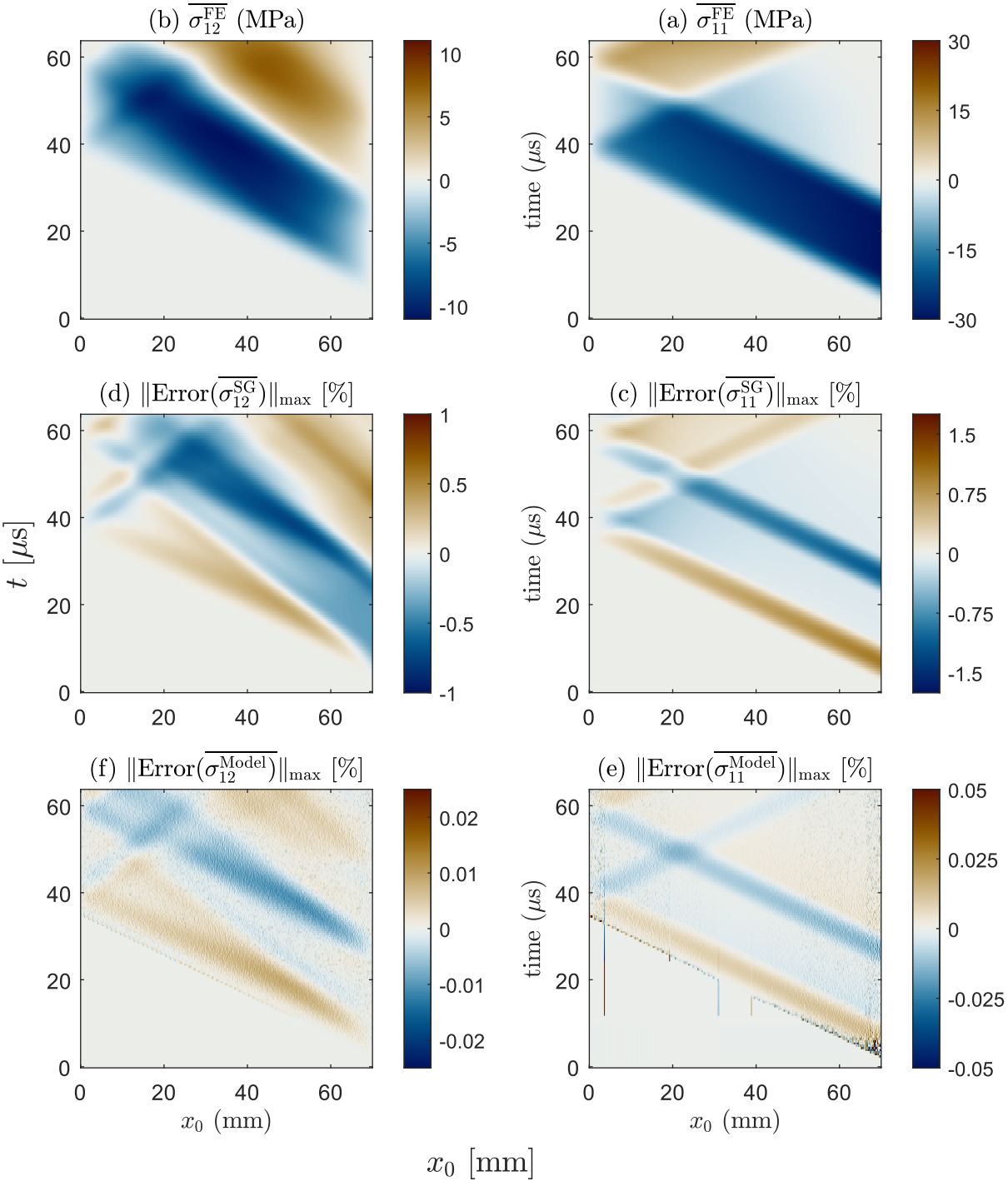

FIGURE 4 $x - t$ diagrams of (a,b) average stress magnitudes output by the finite element simulation, (c,d) normalized errors in stress calculated with the stress gauge equations using finite element accelerations, and (e,f) normalized errors in the stress reproduced with the constitutive model from finite element strain outputs.

G_1^{Ident} [GPa]	Error(G_1^{Ident}) [%]	K_1^{Ident} [GPa]	Error(K_1^{Ident}) [%]	τ_1^{Ident} [µs]	Error(τ_1^{Ident}) [%]
0.888	1.22	1.52	−1.23	9.83	−1.68

TABLE 2 Identified viscoelastic constitutive parameters from finite element kinematic fields.

3.3 | Parameter identification from finite element data

To verify the viscoelastic parameter identification procedure, the acceleration and strain fields, output from the model described in Section 3.1, were extracted every half microsecond for 128 frames. As in Section **??**, the sampling rate was selected to match the temporal resolution of a Shimadzu HPV-X1 UHS camera. These kinematic fields were then used to extract the constitutive parameters according to the procedure outlined in Section 2, and table 2 presents the identified constitutive parameters alongside their identification errors. For a given parameter, Q^{Ref}, the error in the identified parameter, Q^{Ident}, is given by

$$\text{Error}\,(Q) = \frac{Q^{\text{Ident}} - Q^{\text{Ref}}}{Q^{\text{Ref}}} \times 100\%. \tag{10}$$

Successful parameter identification was achieved for all three Maxwell parameters with the largest absolute error found in the extraction of time constant. As discussed in 3.2, the likely source of the parameter identification error from finite element data are temporal discretisation of the kinematic fields. Additionally, to test the stability of the identification to varying initial guesses, the identification was performed using 30 randomly generated initial guesses over the interval $0.75Q^{\text{Ref}} \leq Q^{\text{Guess}} \leq 1.25Q^{\text{Ref}}$, and the identified parameter was extracted from the initial guess producing the smallest value of the cost function. Identification for all constitutive parameters remained stable with the highest standard deviation of $\pm 0.04\%$ found in the bulk modulus and the smallest standard deviation found in the extraction of time constant at 0.02%. This consistency suggests that well defined global minima in the cost functions exist around the reference input parameters.

4 | SIMULATION OF EXPERIMENTAL SOURCES OF ERROR

Having verified the constitutive parameter identification method on finite element data, the next step in the experimental design process is to replicate the additional error resulting from experimental conditions. Major sources of systematic error include the spatial and temporal resolution of the camera and quantitative imaging technique used, along with with biases imparted by preprocessing of the obtained kinematic fields and by measurement noise. The random component of error is dominated by the noise in grey levels of the images captured by the camera.

To quantify the error imparted through the experimental measurement of deformations, we implement a digital replica approach. In this technique, presented graphically in Figure 5, a computer algorithm is used to generate a synthetic image of a gridded sample, with a spatial resolution matching that of the camera and grid intended to be used for an experiment. This grid

I_0	A	b (bits)	p $\frac{\text{mm}}{\text{period}}$	$Resolution$ (pixels)	p_{px} ($\frac{\text{pixels}}{\text{period}}$)	$FrameRate$ (fps)	$\#\ of\ Frames$
0.50	0.25	16	0.90	$[400 \times 250]$	5.00	2.00×10^6	128

TABLE 3 Imaging parameters used in the synthetic image deformation procedure.

image is then synthetically deformed using the time-resolved displacement fields, output by the finite element model described in Section 3, with the temporal resolution matching the frame rate of the camera. The resulting images are then processed using the same procedures that would be used to process the images obtained in an experiment, and the constitutive parameters are extracted. The analysis is repeated while also incrementally adding additional sources of error, including data preprocessing and grey level noise.

Using the finite element model as a basis for deforming computer-generated images presents clear advantages when compared to using experimental images since the underlying constitutive parameters are known. This method allows for the input parameters in the constitutive model to be used as a baseline, enabling the quantification of error propagation through the experimental full-field measurement technique and inverse identification. For further reference, this synthetic image deformation technique is described extensively in the literature[17,23] for multiple full-field measurement methodologies.

4.1 | Synthetic image deformation

For an image based inertial impact test, the data comes in the form of grey-scale images instrumented with a quantitative full-field imaging pattern. In this work, deformation data was obtained via the grid method. This technique involves printing a regular rectangular grid pattern on the specimen and measures displacements from the changes in the spatial frequency of the grid pattern. The experiment is simulated through the deformation of computer-generated grid images according to the finite element deformations.

The specific details of the synthetic image deformation process have been extensively described in the literature[17,23], so only a brief discussion is presented here. First, an undeformed image is generated from a two dimensional symmetric sinusoidal gray-level distribution function with a period equal to the grid pitch, p. The image is then deformed through the substitution of the $\mathbf{x}_1$ and $\mathbf{x}_2$ pixel coordinates with their deformed locations. These deformations are taken from finite element simulations with the displacements of the nodes interpolated to the corresponding pixel locations. The parameters of the image, chosen to simulate images of a 70 mm $\times$ 44 mm specimen captured with a Shimadzu HPV-X1 camera, are presented in Table 3. In the table, the mean gray-level intensity as a fraction of the dynamic is given by I_0 with amplitude A. The grid pitch on the simulated sample, p, is measured in mm, and the resulting pitch on the camera sensor, p_{px}, is the sampling rate in $\frac{\text{pixels}}{\text{period}}$.

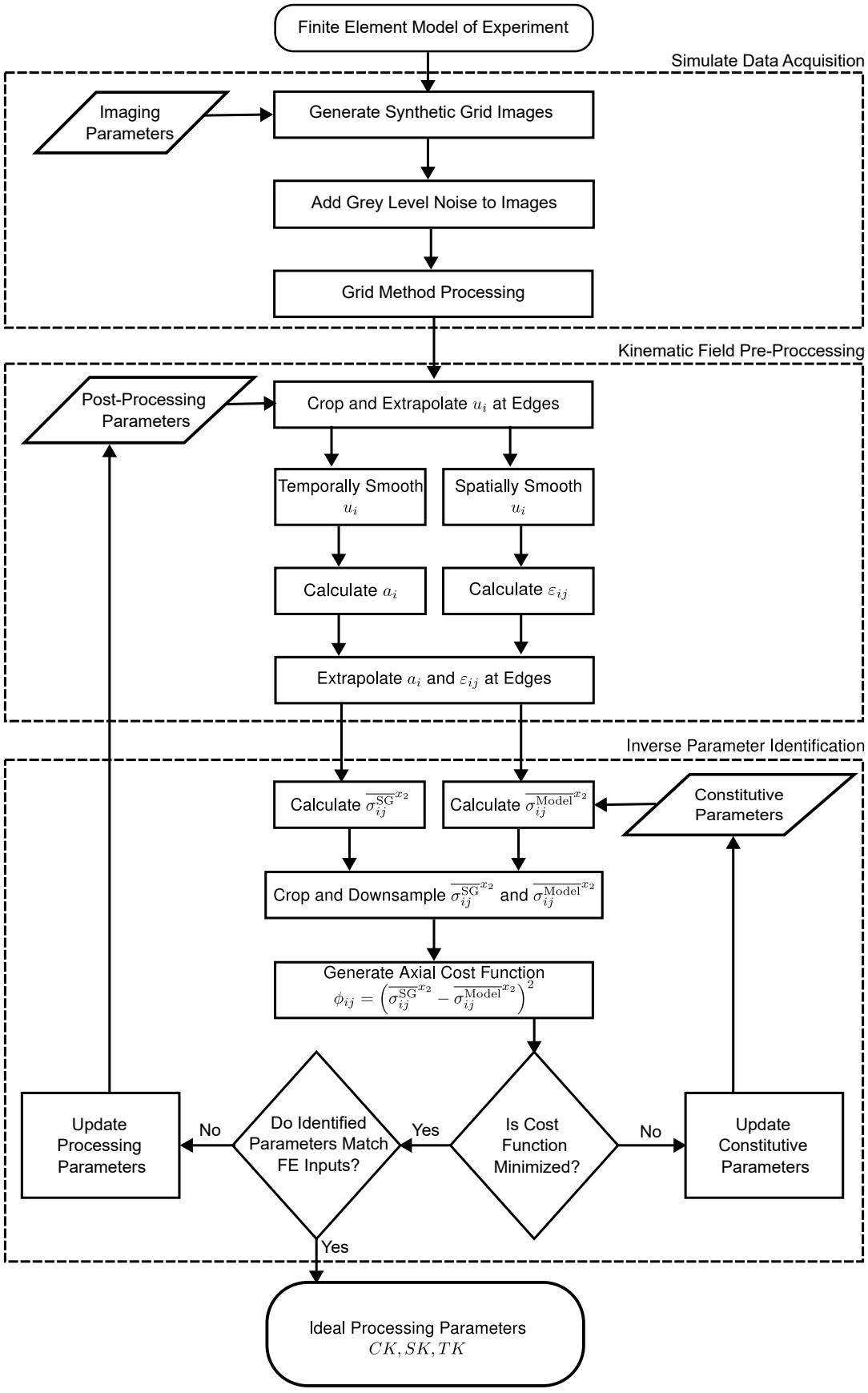

FIGURE 5 A graphical representation of the process for using a digital replica to determine optimal experimental data processing parameters.

4.2 | gray-level noise addition

In a physical experiment, there will always be a degree of measurement uncertainty due to the nature of digital imaging. For example, Johnson-Nyquist noise arising from random thermal motion of charge carriers in camera circuitry manifests as Gaussian noise in the measured gray-level intensity of the images[41]. This noise propagates through the identification procedure as spurious displacements measured through the grid method and results in a possible noise-induced bias and some level of random error in the identification of the constitutive parameters. In this work, measurement noise is simulated through the addition of a random gray-level intensity with a Gaussian probability distribution centered on a mean value of 0 with a standard deviation of $\pm 0.4\%$ of the dynamic range applied to each pixel of the image. This average noise magnitude is selected to match the average noise level of the shimadzu HPV-X1 UHS camera that will be used in upcoming physical experiments. To investigate the effects of this measurement noise on parameter identification, the following analyses are performed on the noisy images along with the original synthetic images.

4.3 | Displacement measurement with the grid method

For this work, the grid method was chosen as the quantitative imaging technique because it offers superior spatial resolution compared to the more common digital image correlation (DIC) technique[25,42,43]. In contrast with DIC, the grid method utilizes a regular periodic grid deposited on the specimen rather than a random speckle pattern[43]. Displacements are then obtained from analyzing the change in phase in that regular gird. For perfect grids and displacements significantly smaller than one grid pitch, this relationship between that phase change and the corresponding displacement can be approximated with

$$u_i = -\frac{p}{2\pi}\Delta\Phi_i. \tag{11}$$

Here, p is the grid pitch, and $\Delta\Phi_i$ represents the phase change in the i^{th} direction. In practice, however, displacements often exceed one grid pitch, and physical grids often contain defects. These cases require an iterative approach to extracting displacements from grid deformations and an unwrapping of the grid phase. These mathematical formulae are omitted here for brevity, but are discussed in detail in Grediac et al.'s review of the grid method[25]. The in-plane strains are then calculated using the infinitesimal strain-displacement relations, and the in-plane accelerations are obtained by differentiating twice in time.

4.4 | Kinematic field preprocessing: edge cropping and extrapolation

In order to utilize the displacement fields extracted with the grid method for inverse constitutive parameter identification, additional processing must be performed. Similar to how digital image correlation returns erroneous displacement data within a subset of the edges of the region of interest[44–46], the grid method processing produces corrupted displacement measurements

within one pitch of the grid edges. Additionally, once the shear strain introduced by the half height impact reaches the edges of the specimen, the induced rotations can lead to orders of magnitude in error in measured strains at the specimen edges. When included in the analysis, these inaccurate strain measurements can lead to large errors in the constitutive parameter identification. Therefore, a correction of the kinematic fields along the specimen edges was implemented.

In previous investigations, simply padding the corrupted data at the edges with those replicated from the closest valid data point to the grid edges has been sufficient to enable parameter identification[18,45,46]. However, such a simplistic approach was found to be insufficient for half-height impacts on viscoelastic materials. A simple replication of valid data does not satisfy the boundary condition of $\varepsilon_{12} = 0$ on the top and bottom free surfaces resulting in errors in shear stress identification. These small errors at the edges are then further propagated and amplified in the bulk modulus identification through the calculation of ε_{33} resulting in poor extraction of K_1. Therefore, a padding scheme that more closely approximates the kinematic field distributions at the edges must be utilized.

Upon further investigation, it was found that the identification errors caused by corrupted edge data could be reduced by first cropping the displacement fields over an interval CK ≥ 7 pixels in from all edges of this displacement fields. The cropped data was then replaced with a quadratic extrapolation of the average displacement gradient $4p$ in from the cropped region. However, in practice measurement noise in the gray-level images necessitates smoothing of the displacement fields in space before calculation of the strain fields. This smoothing propagates noise through the extrapolated fields, sometimes necessitating larger extrapolation intervals than the minimum kernel CK $= 7$ pixels. The next sections discuss the effects of noise and smoothing on the necessary edge extrapolation.

4.5 | Kinematic field preprocessing: spatial smoothing and strain calculation

In a physical experiment, some amount of noise will exist in the grey levels of the images. This grey level noise is amplified by differentiation when calculating the full-field strains. Therefore, the next step is to spatially smooth the displacement fields prior to calculating the strain fields, to mitigate the effects of the noise. This Gaussian spatial smoothing is performed over a kernel SK using the $imgaussfilt$ function in Matlab[39]. The smoothed displacement is then used to calculate strain.

A consequence of the Gaussian smoothing is that displacement noise can be pulled into the extrapolated region if the smoothing kernel is significantly larger than the extrapolation kernel. Additionally, the extrapolated region contains some amount of systematic error that can be propagated through smoothing into the valid region of displacement measurement. Therefore, an ideal relationship between CK and SK must be established.

For SK $\geq$ 15 pixels, the ideal relationship between extrapolation region and smoothing kernel is CK $= \frac{1}{2}$SK. Smaller extrapolation kernels result in the smoothing kernel propagating noise into the extrapolated region resulting in poor parameter

identification. When SK < 15 pixels the systematic error resulting from the poor quality edge data dominates and the minimum extrapolation CK $= 7$ pixels must still be used.

After extrapolation and smoothing of the displacement fields, the infinitesimal strains are calculated. The resulting shear strains are then linearly extrapolated to 0 at the free surfaces to obey the stress-free boundary conditions. Additionally, to suppress any propagation of amplified strain noise from the valid region into the extrapolated region, the normal strains are linearly extrapolated according to the average strain gradient measured over the $4p$ in from the extrapolated region.

4.6 | Kinematic fields preprocessing: temporal smoothing and acceleration calculation

Similarly to how spatial differentiation amplifies displacement noise in the calculation of strain, the temporal differentiation amplifies the displacement noise when calculating the acceleration fields. So, the raw displacement data are independently temporally smoothed using the with a kernel of TK frames to reduce the resulting noise in the accelerations. The temporal smoothing is performed with a third order Savitsky-Golay filter using the *sgolayfilt* Matlab function [39]. Accelerations are calculated through a double temporal differentiation of the smoothed displacement field using a centered finite difference algorithm. The accelerations are then used to calculate the stress gauge stresses using Equations 4 and 4b.

Unlike spatial smoothing, the temporal smoothing kernel and the extrapolation interval are uncoupled. Therefore, the ideal relationship between CK and TK cannot be logically derived. Instead, CK is determined by the size of the spatial smoothing kernel to minimize the systematic deviations between stresses calculated from the constitutive model and those calculated with the stress gauge equations. However, upon the addition of noise, the spatial distribution of accelerations at the edges deviates further from its true value. This deviation worsens with larger extrapolation kernels and increases the random error in the stress gauge stresses. At the same time, temporal smoothing can mitigate this random error over time. Therefore, for noisy images, like those obtained from experiments, larger temporal smoothing kernels may be necessary for larger extrapolation intervals.

5 | IDENTIFICATION VERIFICATION USING SYNTHETIC IMAGES

Constitutive parameter identification is performed on the newly conditioned data in the same manner as on the finite data presented in Section 3. The following sections present an analysis on the systematic error introduced by smoothing of the displacement data followed by the effects of grey level noise on the identification accuracy.

5.1 | Systematic identification error in noise-free images

To investigate the effects of systematic errors introduced by the grid method imaging and data processing on the identification of viscoelastic constitutive parameters, a parametric study was performed on the noise-free synthetic images from Section 4.1.

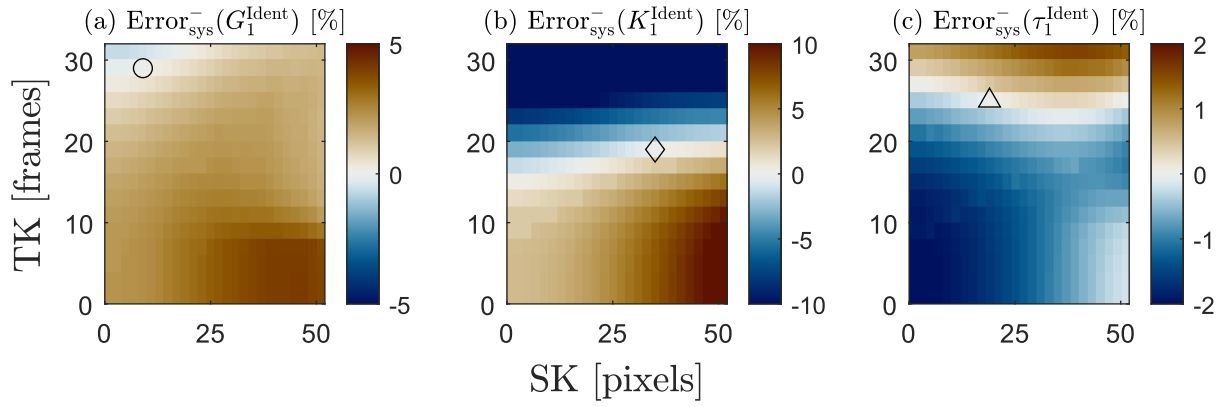

FIGURE 6 Systematic errors in viscoelastic constitutive parameter identification on using noise-free synthetic images. Smoothing kernel pairs resulting in the minimum magnitude of systematic error are called indicated by an open marker symbol.

The kinematic fields were then extracted and conditioned according to the method outlined in Section 4.3 across a parametric sweep of spatial kernels $0 \leq \text{SK} \leq 51$ pixels with the ideal extrapolation kernel described in Section 4.5 and temporal smoothing kernels $0 \leq \text{TK} \leq 31$ frames. To prevent the temporal smoothing from propagating erroneous accelerations forward in time, $\frac{1}{2}$TK frames were cropped from the beginning of the kinematic fields, and the last four frames were cropped from the kinematic fields to minimize errors in the calculation of acceleration from the centered finite different algorithm.

After preprocessing, the kinematic fields were input into the identification algorithm described in Section 2.4 to extract the viscoelastic parameters. Recalling from Figure 4 that errors in the stress gauge algorithm are largely concentrated along the impact edge of the specimen, and that accurate displacement data are lost along the grid edges, the cost functions were only evaluated over the interval $1.8 \text{ mm} \leq x_0 \leq 61\text{mm}$. The systematic identification errors, $\text{Error}^{-}_{\text{Sys}}$, were calculated using Equation (10). To reduce errors caused by poor reconstruction of ε_{33} while remaining representative of an experimental constitutive parameter identification, G^{Ident} corresponding to the pair of smoothing parameters resulting in the minimum absolute systematic error was used to calculate out of plane strains during the minimization of ϕ_{11}.

Figure 6 presents heat maps of the identification errors for the model parameters as functions of SK and TK, and Table 4 lists these extracted properties along with their associated systematic errors (with no smoothing). Without smoothing, identification errors are of comparable, but greater, magnitudes to those identified from finite element kinematic fields. The increase in identification errors from images compared to those from finite element fields is dominated by the systematic errors in the edge extrapolation.

Figure 6 demonstrates that both G_1 and τ_1 are relatively insensitive to spatial and temporal smoothing in the absence of camera noise. The maximum identification error in G_1^{Ident} was calculated at 4.08% with smoothing kernels SK = 45 pixels and TK = 0 frames, and the maximum magnitude for τ_1^{Ident} was calculated to be -2.06% with no smoothing. However, K_1 is demonstrated to be significantly more sensitive to smoothing than either G_1 or τ_1, with the identification converging on the lower

G_1^{Ident} [GPa]	$\text{Error}_{\text{Sys}}^{-}(G_1^{\text{Ident}})$ [%]	K_1^{Ident} [GPa]	$\text{Error}_{\text{Sys}}^{-}(K_1^{\text{Ident}})$ [%]	τ_1^{Ident} [μs]	$\text{Error}_{\text{Sys}}^{-}(\tau_1^{\text{Ident}})$
0.897	2.25	1.58	2.69	9.79	−2.06

TABLE 4 Identified viscoelastic constitutive parameters and associated systematic errors obtained from noise-free synthetic images without smoothing.

boundary of $0.75G_1^{\text{Ref}}$ at a temporal smoothing kernel of TK = 31 frames. For both moduli, identification error increases more rapidly for SK ≥ 15 pixels, further indicating that systematic identification error is driven by the edge extrapolation algorithm.

For all constitutive parameters, a significant amount of temporal smoothing is required to attain the minimum absolutes systematic error in the extracted property. However, no pair of smoothing kernels exists in which any two parameters of interest are minimized, supporting the need for differing smoothing requirements for identification of bulk and shear moduli. Although, at all locations where the absolute error in both G_1 and K_1 are within the absolute error obtained directly from finite element fields, $\left|\text{Error}_{\text{sys}}^{-}\left(\tau_1^{\text{Ident}}\right)\right|$ also lies within the absolute finite element error. Therefore, without noise, the time constant can be reliably extracted at any smoothing kernel from which bulk modulus can also be obtained. Having demonstrated the capability of an IBII test to extract viscoelastic parameters with in the absence of measurement noise, the next step is to determine the optimum set of smoothing parameters when a realistic amount of noise is added to the simulated experimental images.

5.2 | Noise Sensitivity

To investigate the effects of measurement noise on identified constitutive parameters, the same parametric sweep of smoothing parameters as in Section 5.1 was repeated on synthetic images polluted with the addition of gray-level noise in the manner described in Section 4.2. In order to separate the systematic and random contributions of sensor noise, the sweep of parameter extraction across smoothing parameters was carried out on 30 distinct copies of noise. The identification errors from noisy images consist of systematic and random components, given by $\text{Error}_{\text{sys}}^{+}\left(Q^{\text{Ident}}\right)$ and $\text{Error}_{\text{ran}}\left(Q^{\text{Ident}}\right)$, respectively. The systematic component of error is defined as the mean error over the 30 noise copies, the standard deviation gives the random error, and the total error is given by $\text{Error}_{\text{tot}}\left(Q^{\text{Ident}}\right) = \left|\text{Error}_{\text{sys}}^{+}\left(Q^{\text{Ident}}\right)\right| + 2\text{Error}_{\text{ran}}\left(Q^{\text{Ident}}\right)$.

Figure 7 presents the systematic (a-c), random (d-f) , and total (g-i) parameter identification errors calculated from the noisy images. To better compare identification error from noisy images with those obtained using noise-free images, the color scales are truncated to match those from Figure 6. Extraction of K_1^{Ident} and τ_1^{Ident} was performed using the mean value of G_1^{Ident} obtained using the smoothing kernels resulting in the minimum $\text{Error}_{\text{tot}}\left(G_1^{\text{Ident}}\right)$.

If no noise induced bias was present in the identified parameters, $\text{Error}_{\text{sys}}^{+}$ would exactly match $\text{Error}_{\text{sys}}^{-}$ from Figure 6 for all parameters and smoothing kernels. While the systematic error plots with and without noise appear qualitatively similar, it is also apparent that image noise induces a bias in parameter identification when the displacement fields are under-smoothed.

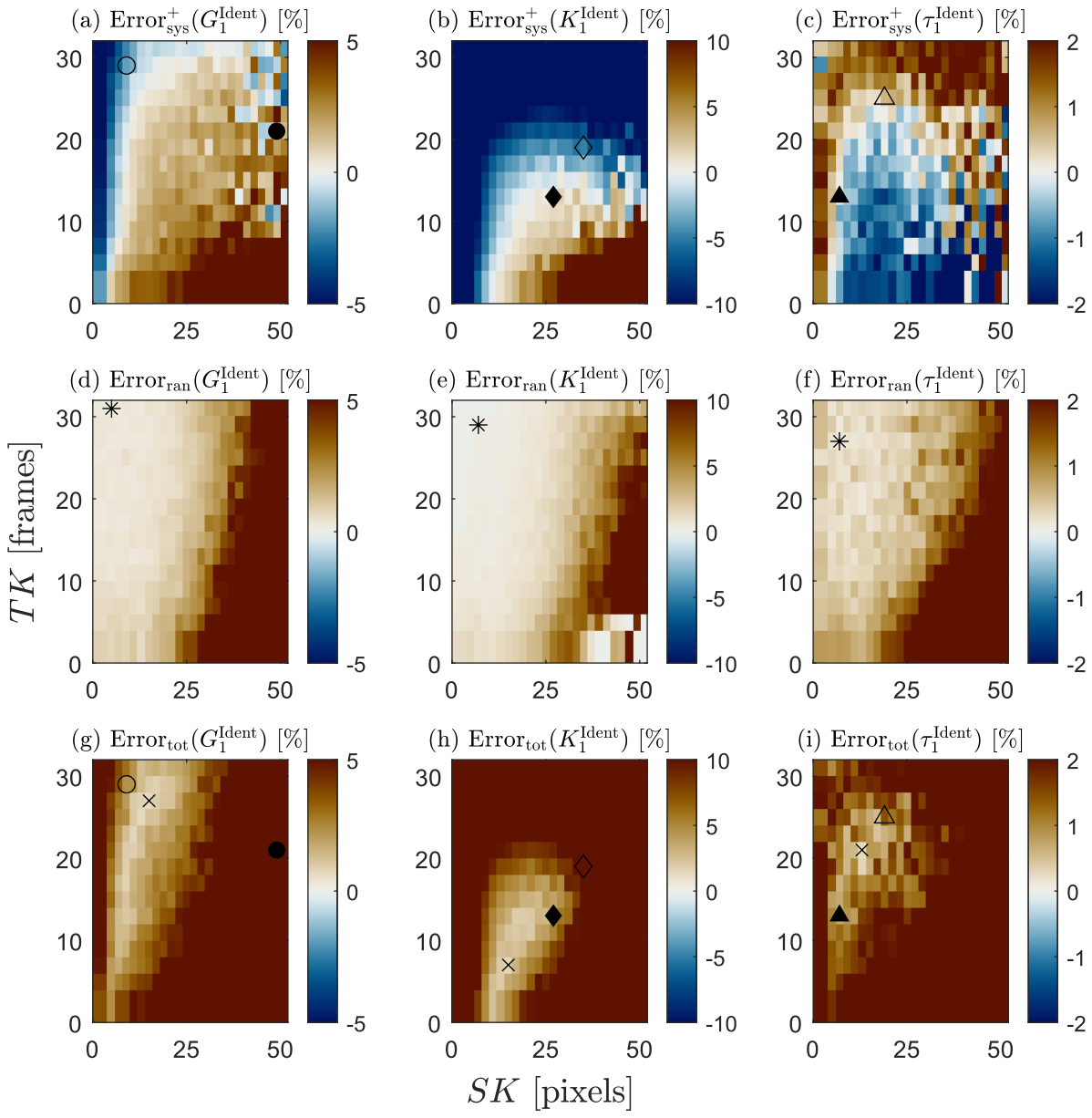

FIGURE 7 Viscoelastic parameter identification errors obtained from a parametric smoothing sweep on noisy synthetic images. Smoothing kernels with the minimum absolute systematic error for noise free images are marked with an open symbol, the corresponding closed symbol indicates the lowest systematic error from noisy images, an * marks minimum random error, and the minimum total error is indicated by an x.

This bias is particularly evident for bulk modulus with $\text{Error}^{+}_{\text{sys}}\left(K_1^{\text{Ident}}\right) \geq 20\%$ when SK $<$ 5 pixels. For smoothing kernels SK $>$ 5 pixels all parameters exhibit stronger sensitivity to spatial smoothing with noise than without. At smaller smoothing kernels, 5 pixels $\leq$ SK $\leq$ 15 pixels, $\text{Error}^{+}_{\text{sys}}$ converges towards 0 with increasing spatial smoothing at temporal smoothing kernels TK $\leq$ 21 frames for the three constitutive parameters. This heavy influence of spatial smoothing stems from the temporal

integration in the constitutive model. Small disturbances in strain lead to step increases or decreases in $\sigma_{ij}^{\text{Model}}$ that propagate through time and result in poor quality identification.

Although some spatial smoothing is required to prevent temporal propagation of errors in the constitutive law, over-smoothing can also result in poorer identification of constitutive parameters. Systematic error in the identification of K_1 is minimized at SK = 27 pixels with noise compared to 35 pixels without and the minimum systematic error for τ_1 occurs at SK = 7 pixels. Additionally, both shear modulus and time constant identification become unstable at large spatial smoothing kernels, SK > 37 pixels oscillating between under-predictions and over-predictions with smoothing kernel changes of only a couple pixels. The absolute minimum systematic error for G_1 lies at SK = 49 pixels, TK = 21 frames outside the apparent band of stable identification error. However, observed susceptibility to large spatial smoothing kernels is less a function of the Gaussian smoothing than the edge extrapolation algorithm.

The influence of edge corrections on identification quality becomes more apparent in the heat maps for $\text{Error}_{\text{ran}}\left(Q^{\text{Ident}}\right)$ presented in Figure 7 (d-f). When temporally smoothed, the random error behaves as expected and decreases with increasing kernel sizes, and the minimum random error occurs at TK ≥ 27 frames for all three parameters. Similarly, spatial smoothing either reduces or maintains the random error with minimal smoothing windows of SK < 15 pixels. However, random error increases rapidly as the spatial smoothing kernel exceeds 15 pixels and CK increases with it. When SK ≥ 15 pixels and CK > 7 pixels, some of the increased random error can be mitigated by also increasing temporal smoothing kernels, but the minimum total error corresponds to a spatial smoothing kernel SK ≤ 15 pixels in both moduli and the time constant. This dependence on temporal smoothing indicates that errors in the extrapolation of accelerations at the edges, instead of over-smoothing or poor extrapolations of the strain fields, drive the increase in both systematic and random parameter identification errors.

Examining the total error plots in Figure 7 (g-i) it is clear that at low spatial smoothing kernels, and therefore extrapolation regions of CK = 7 pixels, systematic error dominates and small temporal smoothing kernels can be used to identify the constitutive parameters. When SK ≥ 15 pixels and CK > 7 pixels, the random error increases rapidly and larger temporal smoothing kernels are required to reliably identify constitutive parameters. Random error becomes dominant and identification is unreliable, with $\text{Error}_{\text{tot}} \geq 5\%$ for extrapolation kernels CK ≥ 18 pixels for G_1 and CK ≥ 15 pixels for K_1. Additionally, systematic error dominates in the identification of K_1 for large temporal smoothing kernels leading to failed identification at TK > 23 pixels.

5.3 | Parameter extraction from noisy images

Having characterized the effects of noise and smoothing kernels on the error in extraction of constitutive parameters from simulated noisy images, the final step is to determine a criterion to identify which processing parameters should be used to extract constitutive properties in a physical experiment. Two logical choices for identification criterion exist. These choices are

Identification Criterion	G_1^{Ident} [GPa]	$\text{Error}(G_1^{\text{Ident}})$ [%]	K_1^{Ident} [GPa]	$\text{Error}(K_1^{\text{Ident}})$ [%]	τ_1^{Ident} [μs] [μs]	$\text{Error}(\tau_1^{\text{Ident}})$ [%]
Minimum $\text{Error}_{\text{tot}}$	0.878 ± 0.002	0.13 ± 0.28	1.54 ± 0.01	0.03 ± 0.76	9.88 ± 0.05	-1.25 ± 0.48
Acceptable Region	0.879 ± 0.015	0.20 ± 1.72	1.53 ± 0.04	-0.31 ± 2.40	9.89 ± 0.07	-1.14 ± 0.73

TABLE 5 Identified viscoelastic constitutive parameters and associated identification errors defined by $\text{Error}\left(Q^{\text{Ident}}\right) = \text{Error}_{\text{sys}}{}^{+}\left(Q^{\text{Ident}}\right) \pm \text{Error}_{\text{ran}}\left(Q^{\text{Ident}}\right)$

the minimum $\text{Error}_{\text{tot}}$ criterion and the acceptable region criterion. Table 5 presents identified constitutive parameters for both of these three criteria. In this investigation, the mean value plus or minus the standard deviation value of the extracted constitutive property over the 30 noise copies at the identified optimum processing kernels yields the identified constitutive parameter. The identification criteria and their associated optimum smoothing parameters are as follows:

- The minimum $\text{Error}_{\text{tot}}$ criterion chooses the smoothing parameter resulting in the smallest total identification error, marked with an "x" on Figure 7 (g-i). Using this method, the optimal processing parameters for extracting G_1 is determined to be $[\text{CK}, \text{SK}, \text{TK}] = [8 \text{ pixels}, 15 \text{ pixels}, 27 \text{ frames}]$. The optimal extraction of K_1 and τ_1 using the minimum criterion $\text{Error}_{\text{tot}}$ occurs with the processing parameters of $[\text{CK}, \text{SK}, \text{TK}] = [8 \text{ pixels}, 15 \text{ pixels}, 7 \text{ frames}]$.

- The acceptable region criterion performs a parametric sweep of processing parameters where $\text{Error}_{\text{tot}}$ is less than or equal to some acceptable threshold. Here, we define the maximum acceptable error magnitude as the largest absolute systematic error obtained from noise-free images without smoothing (recall Table 4) increased to the next integer. In that case, the acceptable $\text{Error}_{\text{tot}}$ is 3% determined from $\text{Error}_{\text{sys}}^{-}\left(K_1^{\text{Ident}}\right)$. The acceptable region for the shear modulus includes 109 sets of kinematic field conditioning parameters within the region bounded by $7 \text{ pixels} \leq \text{CK} \leq 14 \text{ pixels}$, $5 \text{ pixels} \leq \text{SK} \leq 27 \text{ pixels}$, and $0 \leq \text{TK} \leq 31 \text{ frames}$. The acceptable error region for the identification of K_1 and τ_1 consists of 18 sets of processing parameters bounded by $7 \text{ pixels} \leq \text{CK} \leq 13 \text{ pixels}$, $11 \text{ pixels} \leq \text{SK} \leq 25 \text{ pixels}$, and $0 \leq \text{TK} \leq 15 \text{ frames}$ where both $\text{Error}_{\text{tot}}\left(K_1^{\text{Ident}}\right)$ and $\text{Error}_{\text{tot}}\left(\tau_1^{\text{Ident}}\right)$ are less 3%.

When comparing the two identification criteria, both produced similar results with overlapping identification errors. However, each criterion offers its own advantages and disadvantages. The minimum $\text{Error}_{\text{tot}}$ criterion obtains the most accurate moduli extractions with the smallest standard deviation of all parameters with idealized data. The acceptable region criterion performs worse on idealized data with far larger standard deviations than the minimum $\text{Error}_{\text{tot}}$ criterion. However, because it utilizes a sweep of smoothing parameters where the identification errors are considered acceptable, the acceptable region criterion may provide a more robust identification in an experimental setting.

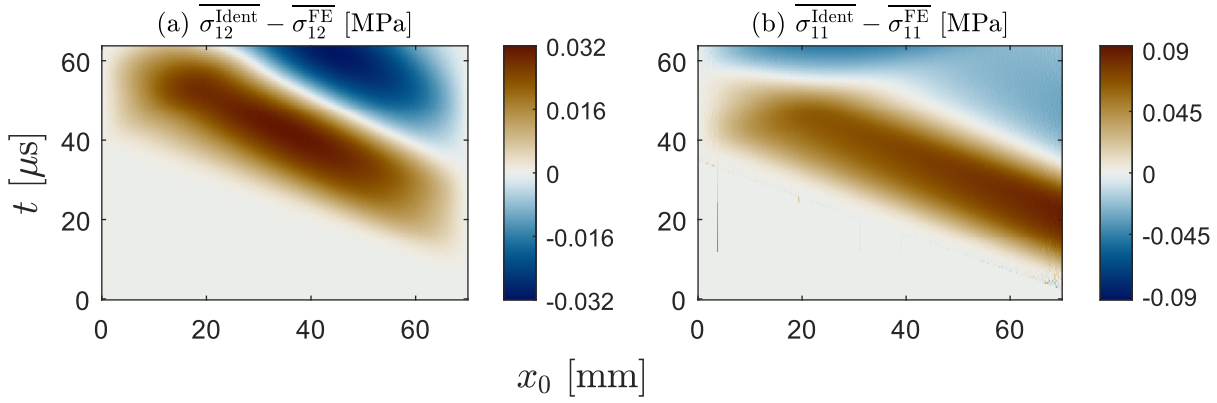

FIGURE 8 Difference between width-averaged stresses calculated identified constitutive parameters using the minimum $\text{Error}_{\text{tot}}$ criterion and those output by the finite element model.

To confirm the quality of the identification, the constitutive parameters identified using the minimum $\text{Error}_{\text{tot}}$ criterion were input into the stress reconstruction algorithm presented in Section 2.3 along with the full-field finite element strains to calculate the constitutive model stresses $\overline{\sigma_{ij}^{\text{Ident}}}$. Figure 8 presents the difference between the width-averaged stresses from the finite element model and those calculated with the ideal identified parameters. Comparing the error maps in Figure 8 with the corresponding maps generated with the reference constitutive parameters in Figure 4 (e) and (f), the error in the stress reconstruction is concentrated on the loading and unloading portions of the pulse when using the reference parameters and on the pulse plateau for the identified constitutive parameters. Additionally, the errors in reconstruction were more randomly distributed in space and time when using reference properties, and more systematic when utilizing extracted parameters. The maximum magnitude of the difference between $\overline{\sigma_{12}^{\text{Ident}}}$ and $\overline{\sigma_{12}^{\text{FE}}}$ was calculated to be 0.093 MPa with a median of 0.004 MPa, compared to a maximum of 0.164 MPa with a median of 0.014 MPa for the stresses calculated using the reference parameters. The extracted constitutive parameters produced a maximum absolute difference of 0.032 MPa with a median value of 0.045 MPa for $\overline{\sigma_{11}^{\text{Ident}}}$, contrasted with a maximum of 5.11 MPa and median of 0.048 MPa for reference constitutive parameters.

To further evaluate the quality of the identified constitutive parameters, a noise floor evaluation was performed to identify what magnitude of displacements, and therefore stress gauge stresses, can theoretically be measured in the simulated experiment. To obtain these measurements, 128 undeformed images are polluted with noise and processed according to the procedure outlined in Section 4. The noise floor, or measurement resolution, is defined as the smallest value for a measured quantity that can reasonably be attributed to mechanical deformation rather than to noise in the camera sensor[47]. Here, this resolution is defined as one standard deviation of the resulting full-field kinematic fields obtained from 128 undeformed noisy images. The noise floors in the displacements, u_i^{NF}, are obtained from the unsmoothed displacement fields and are measured to be $u_i^{\text{NF}} = 1.25$ µm in both the $\mathbf{x}_1$ and $\mathbf{x}_2$ directions. However, the resolution in $\overline{\sigma_{ij}^{\text{SG}}}$ must be determined with the temporal smoothing kernel used to extract the constitutive parameters because accelerations are calculated using temporally smoothed displacements. At the

Recommended Image Acquisition Parameters	
Camera	Shimadzu HPV-X1
Image Resolution	[400 pixels × 250 pixels]
Region of Interest	[389 pixels × 246 pixels] = [70.0 mm × 44.0mm]
Image Scale	0.180 mm/pixel
Frame Rate	2.00×10^6 fps
Grid Pitch	0.900 mm
Grid Sampling	5.00 pixels/period
Recommended Image Processing Parameters	
Grid Method Algorithm	Iterative Grid Method
Image Filtering	None
Edge Extrapolation Kernel	$CK = \begin{cases} 7 \text{ pixels} & if \text{ SK} \leq 15 \text{ pixels} \\ \frac{1}{2}\text{SK} & otherwise \end{cases}$
u_i Extrapolation Order	Quadratic
a_i Extrapolation Order	Quadratic
ε_{ij} Extrapolation Order	Linear
Spatial Smoothing Algorithm	Gaussian
Spatial Smoothing Kernel	$5 \leq \text{SK} \leq 27$ pixels for ε_{12} $11 \leq \text{SK} \leq 25$ pixels for ε_{11} and ε_{22}
Temporal Smoothing Algorithm	3rd order Savitsky-Golay
Temporal Smoothing Kernel	$0 \leq \text{TK} \leq 27$ frames for a_1 $0 \leq \text{TK} \leq 15$ frames for a_2
Predicted Kinematic Field Noise Floors	
Image Noise	0.4%
u_i^{NF}	1.25 μm
$\varepsilon_{11}^{\text{NF}}(\text{SK} = 15 \text{ pixels})$	433×10^{-6}
$\varepsilon_{22}^{\text{NF}}(\text{SK} = 15 \text{ pixels})$	538×10^{-6}
$\varepsilon_{12}^{\text{NF}}(\text{SK} = 15 \text{ pixels})$	537×10^{-6}
$\overline{\sigma_{11}^{\text{SG,NF}}}(\text{TK} = 7 \text{ frames})$	1.24 MPa
$\overline{\sigma_{12}^{\text{SG,NF}}}(\text{TK} = 27 \text{ frames})$	0.177 MPa

TABLE 6 Recommended image acquisition and grid method processing parameters for an IBII test to obtain standard solid model parameters for a viscoelastic material.

temporal smoothing kernel, TK = 27 frames, used to extract shear modulus, the noise floor in $\overline{\sigma_{12}^{\text{SG}}}$ was measured at 0.177 MPa. The noise floor for $\overline{\sigma_{11}^{\text{SG}}}$ was 1.24 MPa at the smoothing kernel TK = 7 frames used to extract the bulk modulus and time constant.

Notably, for both shear and axial stresses, both the maximum and median absolute differences between the finite element stress and reconstructed stresses are smaller using the extracted constitutive parameters than the equivalent differences using the reference values. Additionally, the maximum magnitude of the absolute difference for the shear stress is similar to the noise floor observed in the shear stress gauge stresses. For axial stress, the maximum magnitude of the stress reconstruction error is the same order of magnitude as the stress gauge resolution. These two factors, in combination with the parameter identification errors from simulated experimental images lying within the errors obtained from the finite element kinematic fields, indicate that the IBII test can successfully identify Maxwell parameters for the standard solid model.

Table 6 summarizes the recommended grid method processing parameters for extracting Zener Model constitutive parameters from the simulated IBII experiment. The suggested smoothing and extrapolation kernel sizes are determined using the acceptable region criterion and the reported strain and stress gauge resolutions come from the parameters obtained with the miminum $\mathrm{Error}_{\mathrm{tot}}$ criterion. Although these recommendations are valid for experiments similar to the test simulated herein, they may not apply to experiments that differ significantly, such as those using a different camera, a different loading pulse, or a material that cannot be modeled with a time constant on the order of 10 μs. In these cases, the authors recommend repeating the method outlined throughout this study with the expected imaging and loading parameters to determine the ideal processing parameters for the intended experimental conditions.

6 | CONCLUSIONS

To facilitate improved identification of linear viscoelastic parameters at short time scales and high strain rates, a novel implementation of the IBII test is proposed. The viscoelastic material is modeled using the Maxwell form of the standard solid model, and the constitutive parameters are extracted from the time-resolved full-field deformation data using the stress gauge formulation of the virtual fields method. The experiment is validated with a digital replica approach in which an IBII experiment on a theoretical specimen is simulated using finite elements, and the parameter identification is verified using the output kinematic fields. The finite element data are then used to deform computer-generated grid images matching the spatial and temporal resolutions that would be recorded in a physical experiment, and the resulting kinematic fields are obtained from the images in the same manner as they would be in an experiment. The identification procedure was then performed on the pristine simulated images and then on images polluted with measurement noise to characterize the systematic and random errors. From these simulations it can be concluded that:

- A half-height IBII experiment provides sufficient information to extract viscoelastic bulk and shear modulus along with their associated time constant utilizing a set of two cost functions. First, the shear modulus is extracted by minimizing the difference between the stress obtained from the stress gauge equations and from the constitutive model, and then the process is repeated with the axial stresses. During the calculation of the axial stresses, the identified shear modulus is used to calculate out-of-plane strain.

- The systematic identification error of viscoelastic constitutive parameters is dominated by the poor quality displacement measurements at the sample edges. This corrupted deformation data necessitates the extrapolation of the kinematic fields at least 7 pixels in from the edges to reliably extract constitutive properties, and the spatial smoothing kernel should be at least twice the extrapolation interval.

- The gray-level noise present in experimental images adds a significant systematic bias, as well as a significant random error component in parameter identification. Without spatial smoothing, the temporal integration in the constitutive law propagates errors from noise forward in time and dominates the error in parameter identification. However, as spatial smoothing increases, the random error due to edge extrapolation of the acceleration fields dominates, but can be minimized with increased temporal smoothing.

- The appropriate choice of smoothing parameters can effectively eliminate the systematic error due to noise, and the extraction of the shear and bulk moduli require different smoothing parameters. These ideal smoothing parameters can be defined as the smoothing kernels resulting in the minimum $\mathrm{Error}_{\mathrm{tot}}$. Alternatively, the parameters can be determined from the average identification over a range of smoothing parameters with similar identification error to the systematic error from unsmoothed pristine images. All three criteria were able to successfully identify constitutive parameters to within 3% of their reference values.

With the strong dependence on edge extrapolations and temporal integration of the constitutive law, the largest limiting factor in the use of the IBII experiment to characterize viscoelastic materials is the camera used. As cameras continue to improve over time, increased spatial resolution will allow for higher quality measurement of the displacement fields near the specimen edges, reducing the impact of the edge extrapolation on identification quality. Similar, increases in temporal resolution and record length will enable identification of a wider range of time constants, and more accurate measurement of the relaxation in the material.

Having developed the theoretical framework for the utilization of the image based inertial impact test, the next step is to apply the recommendations made here to the experimental characterization of a viscoelastic material. The next installment of this series will validate the methodology presented here on experimental data.

ACKNOWLEDGMENTS

Research was sponsored by the Army Research Laboratory and was accomplished under Cooperative Agreement Number W911NF-21-2-0027 . The views and conclusions contained in this document are those of the authors and should not be interpreted as representing the official policies, either expressed or implied, of the Army Research Laboratory or the U.S. Government. The U.S. Government is authorized to reproduce and distribute reprints for Government purposes notwithstanding any copyright notation herein. This work has been part-funded by the EPSRC Energy Programme [grant number EP/W006839/1]. The scientifically derived and perceptually uniform color-maps used throughout this work were obtained from a publicly available MATLAB script.[48,49]

References

[1] H. F. Brinson, L. C. Brinson, *Polymer engineering science and viscoelasticity: An introduction*, Springer, **2008**.

[2] J. C. Simo, T. J. R. Hughes in *Computational Inelasticity*, of *Interdisciplinary Applied Mathematics*, J. C. Simo (Ed.), Springer, **1998**, pp. 336–373.

[3] R. S. Lakes, *Viscoelastic solids*, of *CRC mechanical engineering series*, CRC Press, **1999**.

[4] T. Meidav, *Geophysical Prospecting* **1964**, *12* (1), 80–99.

[5] W. Flugge, *Viscoelasticity*, Springer, **2013**.

[6] *ABAQUS/explicit User's Manual, Version 2019*, Dassault Systèmes Simulia Corp, United States, **2019**.

[7] L. Bartolini, D. Iannuzzi, G. Mattei, *Scientific Reports* **2018**, *8* (1), 13697.

[8] M. P. Sepe, *Dynamic mechanical analysis for plastics engineering*, of *PDL handbook series*, Plastics Design Library, **1998**.

[9] V. Burt in *ASM Handbook: Materials Characterization*, *Vol. 10*, A. H. Committee (Ed.), ASM International, **2019**, pp. 320–323.

[10] R. Esmaeeli, H. Aliniagerdroudbari, S. R. Hashemi, C. JBR, S. Farhad, *Modelling and Simulation in Engineering* **2019**, *2019*.

[11] D. Wang, M. Lucas, K. E. Tanner, *Strain* **2013**, *49* (5), 409–419.

[12] F. Pierron, *Strain* **2016**, *52* (3), 186–190.

[13] R. Seghir, F. Pierron, *Experimental Mechanics* **2018**, *58* (2), 183–206.

[14] K. T. Ramesh in *Springer handbook of experimental solid mechanics*, Springer, **2008**, pp. 929–960.

[15] W. W. Chen, B. Song, *Split Hopkinson (Kolsky) bar: design, testing and applications*, Springer Science & Business Media, **2010**.

[16] S. Mousavi, K. Welch, U. Valdek, B. Lundberg, *International Journal of Impact Engineering* **2005**, *31* (9), 1133–1151.

[17] F. Pierron, M. Grédiac, *Strain* **2021**, *57* (1), e12370.

[18] L. Fletcher, J. Van Blitterswyk, F. Pierron, A manual for conducting image-based inertial impact tests, , Technical report, University of Southampton, **2019**, http://dx.doi.org/10.5258/SOTON/P0015.

[19] S. Dreuilhe, F. Davis, C. R. Siviour, F. Pierron in *Advancement of Optical Methods in Experimental Mechanics, Volume 3*, Springer, **2017**, pp. 219–223.

[20] L. Fletcher, F. Pierron, *Journal of Dynamic Behavior of Materials* **2018**, *4* (4), 481–504.

[21] J. Van Blitterswyk, L. Fletcher, F. Pierron, *Journal of Dynamic Behavior of Materials* **2018**, *4* (4), 543–572.

[22] L. Fletcher, J. Van-Blitterswyk, F. Pierron, *Journal of Dynamic Behavior of Materials* **2019**, *5* (1), 65–92.

[23] L. Fletcher, F. Davis, S. Dreuilhe, A. Marek, F. Pierron, *Strain* **2021**, *57* (2), e12375.

[24] L. Fletcher, F. Davis, S. Dreuilhe, A. Marek, F. Pierron, *Strain* **2021**, *57* (2), e12374.

[25] M. Grédiac, F. Sur, B. Blaysat, *Strain* **2016**, *52* (3), 205–243.

[26] F. Pierron, L. Fletcher, *Journal of Dynamic Behavior of Materials* **2019**, *5* (2), 180–193.

[27] J. Van Blitterswyk, L. Fletcher, F. Pierron, *Journal of Dynamic Behavior of Materials* **2020**, *6* (3), 373–398.

[28] F. Pierron, M. Grédiac, *The virtual fields method: extracting constitutive mechanical parameters from full-field deformation measurements*, Springer Science & Business Media, **2012**.

[29] F. Pierron, H. Zhu, C. Siviour, *Philosophical Transactions of the Royal Society A: Mathematical, Physical and Engineering Sciences* **2014**, *372* (2023), 20130195.

[30] P. Bouda, B. Langrand, D. Notta-Cuvier, E. Markiewicz, F. Pierron, *Computational Mechanics* **2019**, *64* (6), 1639–1654.

[31] S. Avril, M. Grédiac, F. Pierron, *Computational Mechanics* **2004**, *34* (6), 439–452.

[32] A. Marek, F. M. Davis, F. Pierron, *Computational Mechanics* **2017**, *60* (3), 409–431.

[33] S. Aloui, R. Othman, A. Poitou, P. Guégan, S. El-Borgi, *Mechanics Research Communications* **2008**, *35* (6), 392–397.

[34] R. Othman, S. Aloui, A. Poitou, *Polymer Testing* **2010**, *29* (5), 616–623.

[35] F. Pierron, P. Forquin, *Strain* **2012**, *48* (5), 388–405.

[36] S. Koumlis, L. Lamberson in *Advances in Experimental Impact Mechanics*, Elsevier, **2022**, pp. 125–149.

[37] C. Zener, *Elasticity and anelasticity of metals*, University of Chicago Press, Chicago, **1948**.

[38] S. Mun, *KSCE Journal of Civil Engineering* **2006**, *10* (3), 195–200.

[39] MATLAB, *version 9.11.0 (R2021b)*, The MathWorks Inc., Natick, Massachusetts, **2021**.

[40] L. Fletcher, F. Pierron, *Experimental Mechanics* **2020**, *60* (4), 493–508.

[41] K. Irie, A. E. McKinnon, K. Unsworth, I. M. Woodhead, *Measurement Science and Technology* **2008**, *19* (4), 045207.

[42] M. Grédiac, B. Blaysat, F. Sur, *Experimental Mechanics* **2017**, *57* (6), 871–903.

[43] H. Schreier, J.-J. Orteu, M. A. Sutton, *Image Correlation for Shape, Motion and Deformation Measurements*, Springer US, **2009**.

[44] M. Rossi, F. Pierron, *International Journal of Solids and Structures* **2012**, *49* (3), 420–435.

[45] P. Wang, F. Pierron, O. T. Thomsen, *Experimental Mechanics* **2013**, *53* (6), 1001–1015.

[46] M. Rossi, P. Lava, F. Pierron, D. Debruyne, M. Sasso, *Strain* **2015**, *51* (3), 206–222.

[47] A. Chrysochoos, Y. Surrel, *Basics of Metrology and Introduction to Techniques*, John Wiley & Sons, Ltd, **2013**, chapter 1, pp. 1–30.

[48] F. Crameri, *Geoscientific Model Development* **2018**, *11* (6), 2541–2562.

[49] F. Crameri, *Scientific Colour Maps*, **2019**. https://zenodo.org/record/1243862.